A Mechanistic Collective Cell Model for Epithelial Colony Growth and Contact Inhibition

S. Aland[1,*], H. Hatzikirou[1,2], J. Lowengrub[3,*], A. Voigt[1,2,4]

[1] Department of Mathematics, TU Dresden, Germany; [2] Center for Advancing Electronics Dresden (CfAED), TU Dresden, Germany; [3] Department of Mathematics and Center of Excellence in Systems Biology, UC Irvine, USA; [4] Center for Systems Biology Dresden (CSBD), Dresden, Germany

Abstract

We present a mechanistic hybrid continuum-discrete model to simulate the dynamics of epithelial cell colonies. Collective cell dynamics are modeled using continuum equations that capture plastic, viscoelastic and elastic deformations in the clusters while providing single-cell resolution. The continuum equations can be viewed as a coarse-grained version of previously developed discrete models that treat epithelial clusters as a two-dimensional network of vertices or stochastic interacting particles and follow the framework of dynamic density functional theory appropriately modified to account for cell size and shape variability. The discrete component of the model implements cell division and thus influences cell sizes and shapes that couple to the continuum component. The model is validated against recent in vitro studies of epithelial cell colonies using Madin-Darby canine kidney cells. In good agreement with the experiments, we find that mechanical interactions and constraints on the local expansion of cell size cause inhibition of cell motion and reductive cell division. This leads to successively smaller cells and a transition from exponential to quadratic growth of the colony that is associated with a constant-thickness rim of growing cells at the cluster edge, and the emergence of short-range ordering and solid-like behavior. A detailed analysis of the model reveals a scale-invariance of the growth and provides insight on the generation of stresses and their influence on the dynamics of the colonies. Compared to previous models, our approach has several advantages: it is dimension independent, it can be parametrized using classical elastic properties (Poisson's ratio and Young's modulus), and it can easily be extended to incorporate multiple cell types and general substrate geometries.

Insert Received for publication Date and in final form Date.

* Corresponding authors: sebastian.aland@tu-dresden.de, lowengrb@math.uci.edu

1 INTRODUCTION

The regulation of cell division, cell sizes and cell arrangements is central to tissue morphogenesis. A detailed understanding of this regulation provides insight not only to the development and regeneration of normal tissues but also to carcinogenesis when regulation breaks down. While regulation of cell division and growth has been traditionally studied via signaling pathways triggered by diffusible chemical species, the importance of mechanical constraints and mechanotransduction is increasingly recognized, see e.g. the review (1) focusing on mechanical forces in epithelial tissue, which provides an important model system to study regulation of cell division, growth and arrangements.

The dynamics of growing epithelial tissues are characterized by a delicate interplay of cell-cell interactions and macroscopic collective motion. In cultures of normal epithelial cells, as the density of cells increases due to proliferation and cell growth, the cells lose their ability to move freely. Mitotic arrest occurs and the cells acquire an epithelial morphology. This process is known as contact inhibition. In (2) detailed in vitro studies of epithelial tissue dynamics using Madin-Darby canine kidney (MDCK) cells were performed and a quantitative analysis of the evolution of cell density, cell motility and cell division rate was presented. It was shown that inhibition of mitosis is a consequence of mechanical constraints that result in reductive cell division, which leads to an overall decrease in cell sizes, rather than just being a consequence of cell contact. Cell growth, division, migration and contact inhibition have also been seen to play a role in glass-like transitions from liquid-like to solid-like behavior in clusters of MDCK cells (3).

Mechanically-based models have been previously used to simulate the dynamics of a collection of epithelial cells in a variety of contexts. For example, a fully continuous description considering the epithelium as an elastic media was considered in (4) where the effect of mechanical stress

0006-3495/08/09/2624/12 $2.00 doi: 10.1529/biophysj.106.090944

on cell proliferation was investigated. While contact inhibition could described qualitatively this formulation prevents quantification at the level of a single cell. Cell-level resolution is achieved in discrete descriptions such as the Cellular Potts model (e.g., (5)) and vertex models (e.g. (6)). In the former, cells are modeled as a collection of grid points on a Cartesian mesh. The system is equipped with an energy that accounts for biophysical properties including adhesion, cell-stiffness and motility and the dynamics occur stochastically using a Boltzmann acceptance function that determines whether two grid points should exchange their properties. The Cellular Potts model (CPM) was recently used to investigate the effects of cell compressibility, motility and contact inhibition on the growth of tumor cell clusters. Interestingly, that in the CPM an artifact was found that an increased motility led to smaller cells, which could only be compensated by increasing the cell stiffness parameters appropriately (7). In the vertex model, epithelial cells are described by a two-dimensional network of vertices, representing the cell edges (see Fig. 1(A) and (B)). Stable network configurations are achieved by a mechanical force balance between an outward force due to limited cell compressibility and an opposing line tension resulting from the combined effect of myosin-dependent cortical contractility and cell-cell adhesion. These forces are incorporated into an energy function that is calculated and used to update the position of each vertex over time. Within this framework, the contributions of cell growth, mitosis, apoptosis and cell intercalation are incorporated to predict the evolution of tissue towards a stable mechanical equilibrium. Vertex models have been successfully used to model processes such as the shaping of compartment boundaries in the developing Drosophilia wing (8), morphogen distribution and growth control (9) among others. It should be noted that in vertex models other mechanical contributions such as cell-matrix adhesion (10), centripetal cytoplasmic contractile activity (11) or the ability of cells to change neighbors, which can be described as tissue fluidity, are either missing or have only incorporated in an ad hoc fashion. Another limitation of most current vertex models is that they are primarily restricted to two-dimensions; extensions to three-dimensions are in the early stages of development (12).

Collective cell motion in epithelial sheets has also been quantitatively described by stochastic particle models, e.g. (13). In this approach, each cell is reduced to its center point (although in a few studies cell sizes have been taken into account, e.g., (14)) and the dynamics are described by Langevin-like systems of equations. The stochastic motion of a cell is modeled by an Ornstein-Uhlenbeck process. Through a linear damping term dissipation due to adhesion and friction is taken into account and the interaction with neighboring cells is modeled by an 'inter-cell' potential that is repulsive at short-ranges and attractive at longer distances. Such models have been able to quantitatively reproduce statistical characteristics of the cell velocity field and positions at early times in controlled wound healing experiments on MDCK cells (15, 16). However, while cell intercalation is naturally included, cell growth, mitosis and apoptosis were either not considered or were only accounted for in an implicit manner by a density-dependent noise term. Further, because cell sizes are not typically taken into account, this makes it problematic to use particle models to simulate reductive cell division.

It is worthwhile to relate stochastic particle models with vertex models, although it is difficult to directly compare the two. A qualitative comparison between these models can be made by constructing the Voronoi diagram for the center points in the particle model, which can then be used to relate epithelial cell packings in the particle and vertex models to one another. See Fig. 1 (C). Our goal here is not to make the link between both approaches quantitative, but rather to use the stochastic particle model as a starting point to derive a coarse-grained continuum model, following the framework of dynamic density functional theory (DDFT). By extending this framework to account for cell size and shape variability, we obtain a continuum partial differential equation for the epithelial cell density that provides single cell resolution and yet can describe elastic, plastic and viscoelastic deformations at larger scales. Such a modeling approach was previously sketched for solid tumor growth in (17), but no simulation results were provided. This approach is motivated by the successes of DDFT in simulating inhomogeneous, non-equilibrium interacting particle systems with Brownian dynamics (18, 19). Because of the continuum formulation, the model extends straightforwardly to three dimensions. The model can easily incorporate other biophysical phenomena, such as flow, nutrient diffusion and active motion via chemotaxis. Unlike the approach described in (17), cell division is accomplished using a discrete approach making the overall system a hybrid continuum-discrete model. We will demonstrate the quantitative predictive power of such a modeling approach by comparing our simulation results with the detailed analysis of contact inhibition in (2).

2 MATERIALS AND METHODS

In the DDFT framework, a discrete particle system is modeled via a continuum-level continuity equation for a noise-averaged density field $\rho(x,t) =< \sum_i \delta(x_i(t) - x) >$, where $< \cdot >$ denotes averaging and $x_i(t)$ denotes the particle positions. A key idea is that the averaged density evolves on experimentally-relevant long-time scales (seconds to hours for representative experimental growth conditions), while still allowing the individual locations of the particles (peaks of the density field) to be determined. The continuity equation accounts for correlations among the particles through a

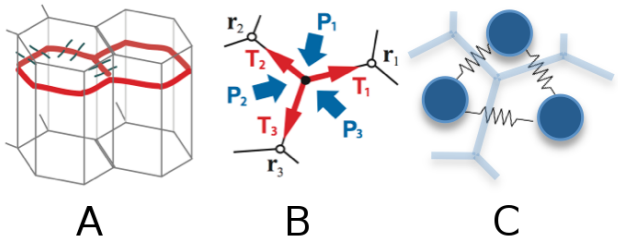

Figure 1: (**A**) A sketch of epithelial cells, for which we assume that the mechanical interactions act in the plane of the adherens junctions. (**B**) Two-dimensional vertex representation of epithelial cells with balancing forces on a vertex due to line tension (red) and pressure (blue). (**C**) Two-dimensional particle representation of epithelial cells with balancing forces represented by springs, and a corresponding Voronoi diagram.

non-local contribution involving the direct two-point correlation function (18) and derives from a gradient flow of a non-local free energy function. Expanding the free energy function to lowest order, the nonlocal equation can be reduced to a high-order partial differential equation, known as the phase field crystal (PFC) model (20, 21). The PFC was introduced as model for elasticity in crystalline structures (22) and is popular in condensed matter physics because of its simplicity and its ability to combine particle-particle interactions with macroscopic material behavior. Here, we adapt the PFC model to account for cell size and shape variability.

2.1 Conserved gradient flow for cell density

Like the DDFT system, the PFC model possesses a free-energy that involves the averaged density ρ as well as parameters that describe the equilibrium epithelial cell packing. The density evolves according to a generalized continuity equation that arises from a conserved gradient flow model. The free-energy expression reads

$$E = \int_\Omega \frac{1}{4}\tilde{\rho}^4 + \frac{1+r}{2}\tilde{\rho}^2 - cq|\nabla\tilde{\rho}|^2 + \frac{c^2}{2}\left[\nabla\cdot(q\nabla\tilde{\rho})\right]^2 \mathrm{d}x, \tag{1}$$

where $\tilde{\rho} = \rho - \bar{\rho}$ denotes the difference between the epithelial cell density and a reference value $\bar{\rho}$. In the remainder of the paper, we omit the tilde and simply use ρ to denote the density difference. The parameter q can be interpreted as the equilibrium epithelilal cell area, which we will make spatially-varying as described below to account for different cell sizes. The parameter r together with the average cell density ρ_0 are used to approximate the 'inter-cell' potential, again with repulsive and attractive interactions. Both parameters are used to fit the first peak in the 'two-cell' direct correlation function and are related to elastic parameters (e.g., Poisson's ratio and Young's modulus) of the epithelial cell cluster, see SI for details. The constant $c = \sqrt{3}/8\pi^2$ is introduced to scale q such that it can be interpreted as the cell area, at least in hexagonal ordering of cells as given by the one-mode approximation, see SI for details. Finally, Ω denotes the domain.

The first two terms in Eq. (1) define a double well potential for appropriate values of r, with two minima corresponding to the presence of a cell or no cell. The third term, a gradient term, can also be found in classical Ginzburg-Landau type models although the sign here is negative, which induces oscillations. The fourth term, which is higher order, stabilizes these oscillations and together with the gradient term sets a length scale, which defines the equilibrium cell size q. For the dynamics we consider a conserved gradient flow

$$\partial_t\rho = \eta\Delta\frac{\delta E}{\delta\rho} \tag{2}$$

where η is a mobility parameter, which can be interpreted as modeling the combined effects of cell-substrate adhesion and friction between the cells and a surrounding viscous fluid. The variational derivative $\frac{\delta E}{\delta\rho}$ is given by

$$\begin{aligned}\frac{\delta E}{\delta\rho} =& \rho^3 + (1+r)\rho + 2c\nabla\cdot(q\nabla\rho) \\ &+ c^2\nabla\cdot(q\nabla(\nabla\cdot(q\nabla\rho))).\end{aligned}$$

We can interpret the (local) maxima in the density field as the centers of the epithelial cells. Within this approach ρ is globally conserved. However, the number of maxima and thus the number of cells is not. If a cell disappears it 'diffuses' into the surrounding cells, leading to a decrease in the maxima and finally its disappearance. To overcome this problem we extend the continuous PFC model by a semi-discrete term taking into account the discrete position of each cell.

Let the cells be numbered by $i = 1, ..., N$ where N is the total number of cells. For cell i, we denote the corresponding local maximum of the density field by ρ_i, and the position of this maximum by x_i, hence $\rho(x_i) = \rho_i$. From the positions of the local maxima, we may compute the Voronoi cells Ω_i, which serve as a good representation of the geometry of the epithelial cell i and can be used to represent the epithelia packing. Correspondingly, we introduce the characteristic function of each cell χ_i defined by $\chi_i = 1$ in Ω_i and 0 otherwise. The region without cells is denoted by $\chi_0 = 1 - \sum_{i=1}^N \chi_i$. In equilibrium, Ω_i and χ_i are related to the equilibrium cell size q, which was assumed to be constant in the original model (22). Here, however, we allow q to be space-dependent to account for cell size variability that can occur during the evolution due to cell division. That is, $q = \sum_{i=0}^N q_i\chi_i$ where q_i is a measure of the epithelial cell area, which can be time-dependent. See the discussion below in Sec. 2.2. In the region without cells ($\chi_0 \approx 1$) we set to $q_0 = 1$

To ensure the number of cells is conserved between mitotic or apoptotic events, we need local 'mass' conservation for each cell. Hence, 'mass' must be added when a local maximum shrinks and 'mass' must be removed when a local maximum grows. The simplest way to do this is to add a source term to the standard PFC model. Hence, we propose the following evolution equation

$$\partial_t \rho = \eta \Delta \frac{\delta E}{\delta \rho} + \alpha \sum_{i=1}^{N} (\rho_{\max} - \rho_i) \max(\rho, 0) \chi_i, \quad (3)$$

where α is a relaxation constant. Equation (3) is designed so that for each cell, the local maximum of ρ stays close to the value $\rho_{\max}$, which approximates the cell density peak at equilibrium and can be a priori calculated from an one-mode approximation, see SI. Note that the evolution equation (3) only prevents disappearance of cells since the source term (last term on the RHS) is restricted to the cell region by χ_i. Analogously, a similar source term is added in the region without cells to ensure that no cells 'nucleate' there. The resulting evolution equation reads:

$$\partial_t \rho = \eta \Delta \frac{\delta E}{\delta \rho} + \alpha \sum_{i=1}^{N} (\rho_{\max} - \rho_i) \max(\rho, 0) \chi_i + \beta (\rho_{\min} - \rho) \chi_0, \quad (4)$$

where β is a relaxation constant and $\rho_{\min}$ is a reference value of the density for the region without cells that can also be estimated from the one-mode approximation, see SI. In the literature on PFC models in condensed matter physics other approaches to ensure a conservation of particles/cells have also been discussed (23, 24). Our results show that the dynamics of the modified PFC model is very similar to that of the original PFC mode. In particular, the source and sink correction terms on the RHS of Eq. (4) at each time step in the numerical scheme are very small because the the diffusional process of disappearance and nucleation of particles/cells is slow compared with other processes. Further, these corrections can be interpreted as penalty terms that seek to maintain the peak values of the density field at $\rho_{\max}$ and the bulk value at $\rho_{\min}$.

2.2 Cell growth, mitosis and apoptosis

We now incorporate cell growth, mitosis and apoptosis. The equilibrium size of each cell may change over time as cells may increase their size until they divide. After division, of course, the equilibrium cell size is reduced abruptly. Prior to division, we assume that there is a cell-dependent rate k_i such that

$$\partial_t q_i = k_i. \quad (5)$$

In the present work, we take k_i to be constant for each cell. More generally k_i may depend on the concentration of available nutrients or growth factors. Here we concentrate on modeling contact inhibition and therefore take into account that in densely packed regions a cell might not have enough space to grow. Comparing the actual cell area $|\Omega_i| = \int \chi_i dx$ with the desired equilibrium cell area q_i, we obtain an approximation for the cell compression (7). If the ratio $\int \chi_i dx / q_i$ is below a threshold value the growth of a cell is prohibited by prescribing $\partial_t q_i = 0$. Here, we take 0.9 as the threshold.

Mitosis can be initiated by different events. In the simulations here, we use the cell life time as a trigger as this is suggested by the experiments in (2). In particular, mitosis initiated in when the cell reaches a prescribed life time $t_i \geq t_{div,i}$, which is taken to be random (see Sec. 3.1). To perform division, we replace the local maximum at x_i with two new maxima using Gaussians in the neighborhood of the original maximum. The position of the new maxima can be chosen in different ways and may affect the cell topology (25). Here we are free to choose any cleavage plane mechanism, but restrict our numerical tests to three different cleavage mechanisms (see Sec. 3.4 and Fig. 5). In each case the daughter cells are put at a distance of $\frac{1}{2\sqrt{\pi}}\sqrt{q_i}$ on opposite sites from the original mother cell and the cell size of the two daughter cells is set such that $q_{child} = q_i/4$, which results from a one-mode approximation, see SI for details. Apoptosis is not considered in the present simulations but can be included easily by removing a cell according to a given criteria like cell age, available nutrients, number of divisions or random selection.

2.3 Numerical algorithm

In the following we briefly mention some details of the numerical implementation of the model. The algorithm for one time step is summarized in Fig. 2. The finite-difference scheme proposed in (26) is employed to solve the PFC equation. For the standard PFC equation this scheme is unconditionally energy-stable. The discretized equations are solved by an efficient nonlinear multigrid method proposed in (27). For the standard PFC equation this algorithm is first-order accurate in time and second-order accurate in space. We obtain similar results for the modified PFC equation used here.

According to the phase diagram of the standard PFC equation we choose $r = -0.9$ together with $\rho_0 = -0.54$. This choice ensures coexistence between a hexagonal epithelial cell packing and a region without cells in equilibrium, with a sharp transition between both phases, see SI for details. The parameters imply that $\rho_{\max} = \rho_{\text{peak}} = 0.8$, the Poisson's ratio is $\nu = 1/3$ and the Young's modulus is $E = 0.4$ (see SI). Since the results are not sensitive to the value of $\rho_{\min}$, we take $\rho_{\min} = -0.7$. Other numerical parameters are time step $\Delta t = 50s$ and grid size $\Delta x = 0.59\mu m$

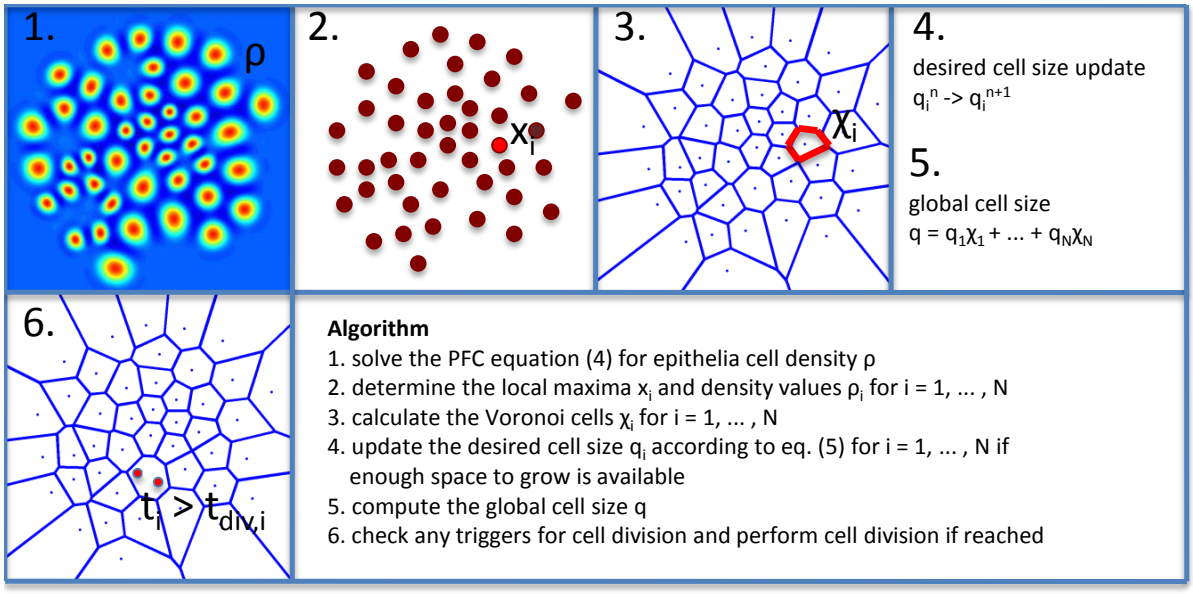

Figure 2: Schematic description of the numerical algorithm. The artifacts of the Voronoi cells at the periphery are only graphical and do not influence the computation.

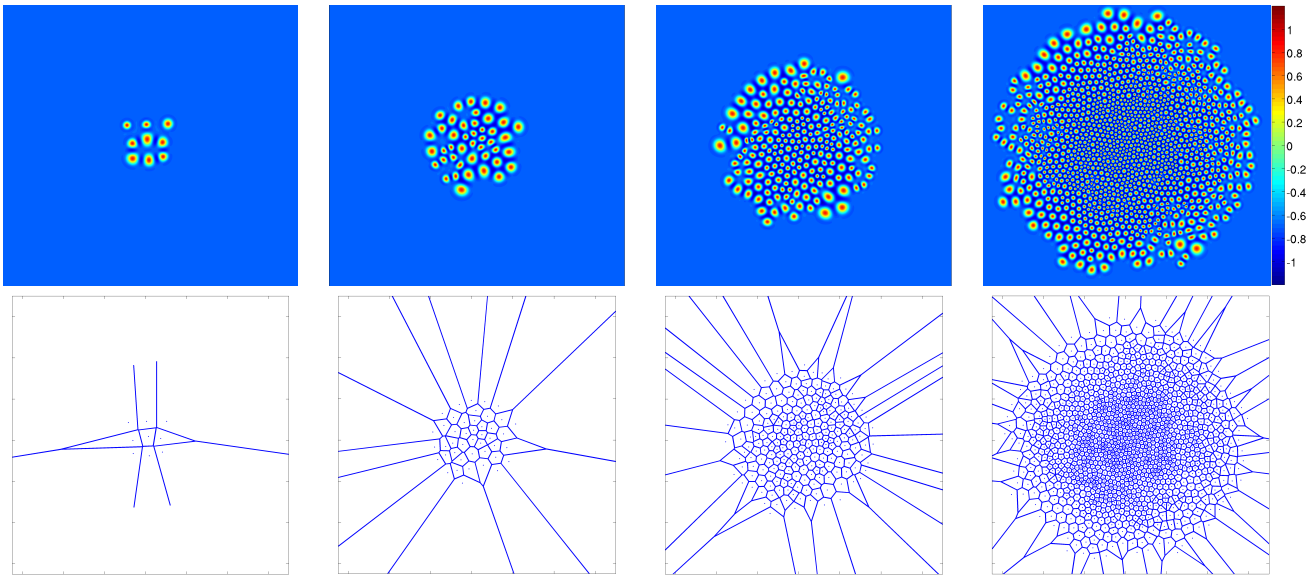

Figure 3: Epithelial cell density field ρ (top row) and corresponding Voronoi diagram (bottom row) at times $t = 0.05d, 1.73d, 3.46d$ and $5.77d$ (from left to right). The artifacts of the Voronoi cells at the periphery are only graphical and do not influence the computation.

and we use $N = 2048$ grid points in each direction. The spatial domain is thus a square with area $1.46mm^2$.

To extract the peak positions from the density field we exploit that peak positions are known from the previous time step. For every i, all grid points in a neighborhood of the old peak position x_i are traversed (here we use the 50 closest grid points). Then x_i is set to the position where ρ assumes the largest value. For the generation of Voronoi cells, the distance to all peak positions is calculated for every grid point and divided by the radius of the corresponding cell. The closest peak position x_i is used to label the grid point belonging to Voronoi cell i.

3 RESULTS

For all simulations we use the nondimensional PFC equations given in Eq. (4) using the characteristic length and time scales $L = 0.59\mu m$ and $T = 50s$. Accordingly, T determines the time step for the numerical scheme and L is small enough to ensure having 100 grid points in cells as small as $35\mu m^2$.

3.1 Simulation setup

We start with a small colony of 9 epithelial cells with areas q_i randomly chosen in the interval $[500\mu m^2, 2000\mu m^2]$ and placed in the center of the computational domain. The division time $t_{div,i}$ after which cell i divides depends on q_i and is motivated by the Hill-function given in (2). The explicit form reads $t_{div,i} = 0.74d(q_i^4 + (170\mu m^2)^4)/q_i^4 + \mathcal{P}([0, 0.02d])$, where $\mathcal{P}(X)$ denotes a random variable uniformly distributed in X and d denotes days. The average cell division time is $0.75d$ for larger cells ($q_i > 170\mu m^2$), while the division time drops rapidly to zero for smaller cells ($q_i << 170\mu m^2$). The cell growth rate is set to $k_i = 2000\mu m^2/d$ which implies that the epithelial cells on average reach the size of their mother cell during cell cycle time if they can freely grow. The remaining parameters are in nondimensional form: $\alpha = 1, \beta = 1$ and we vary η from 5 to 20.

3.2 Growth experiments

Fig. 3 shows snapshots of the density field ρ describing the epithelial cell positions at various times and the corresponding Voronoi diagrams that characterize the cell packings. The colony expands over time, which is enabled by repulsive forces between the epithelial cells, where cells push their neighbors away as they grow. A cluster of $1,369$ cells has developed at final time, with smaller cells in the inner region and larger cells in the outer region.

3.3 Growth characteristics

An analysis of the numerical results is shown in Fig. 4, together with comparisons with experimental results from (2). In Fig. 4(A), the evolution of the colony areas is shown for the simulation results with different mobilities η, and the experimental results (circles). The experimental and simulation results are scaled as described below, and are in excellent agreement. Reference results are shown for exponential growth (solid black) and quadratic growth (solid grey). The results show that there is a transition at about $2d$ from exponential growth to quadratic growth. This can be explained as follows. At early times, since all cells may grow and divide, the cluster area A grows exponentially: $dA/dt \sim \lambda A$, where $\lambda^{-1} \sim 0.75d$, the average epithelial cell cycle time. As the cluster grows, mechanical constraints (contact inhibition) due to reduced cell movement and the lack of space prevent the interior cells from growing in size although interior cells continue to divide by reductive cell division until their size drops below the critical threshold. This leads to larger numbers of smaller cells, with the total areas being approximately conserved. The growth in size in the colony is due to a ring of growing and proliferating cells at the colony edge, leading to a colony growth law $dA/dt \sim 2\sqrt{\pi}\lambda r_{rim}\sqrt{A}$, where r_{rim} is the thickness of the proliferating rim. Thus at late times, $A \sim \pi\lambda^2 r_{rim}^2 t^2$. This analysis reveals a scaling invariance: If $A(t)$ is a solution of the growth law, then $\bar{A}(\bar{t}) = A(t + t_{shift})/A_{ref}$ is also a solution of the growth law with corresponding rim thickness $\bar{r}_{rim} = r_{rim}/\sqrt{A_{ref}}$. Thereby, $t_{shift} = -\lambda^{-1}\ln(A_{ref})$ since the time span of exponential growth increases by t_{shift}. Hence, there is effectively only one free variable (A_{ref} or t_{shift}) to fit. We take advantage of this scale invariance to compare the simulated and experimental results. In Fig. 4(A) the scaled results $\bar{A}(\bar{t})$ are plotted as a function of $\bar{t}$ for the different cases where A_{ref} is chosen empirically to match the $\eta = 10$ simulations. For example, in the experiments, the colony area is approximately 30 times larger than the one obtained for $\eta = 10$ simulation. By considering $A_{ref} = 30$ we calculate $t_{shift} = 4.5d$. We find $\bar{r}_{rim} \approx 70\mu m$, which corresponds to a proliferating rim thickness in the experiments $r_{rim} \approx 385\mu m$. Similar scalings are used for the numerical results. In particular, increasing the mobility η leads to larger cluster sizes, delays the transition from exponential to quadratic growth by making the cells more mobile and thus extends the regime of free-growth (see SI). As also shown in the SI, increasing the Young's modulus has a similar effect.

During the exponential phase of growth, the cell density (Fig. 4B) and the cell sizes on average (Fig. 4C), and for an individual cell (Fig. 4D), remain nearly constant. That is, daughter cells have approximately the same areas as mother cells. After $\bar{t} \approx 2d$ growth is inhibited and expansion of the colony periphery cannot keep up with cell proliferation in the bulk. Hence the density of bulk cells increases due to the limited space and the cell sizes decrease due to reductive cell division where the interior daughter cells have approximately one-half of the area of the mother cells, in agreement with the experimental measurements (see Figs. 3C and 4A in (2)).

3.4 Cell arrangements

To quantify the cell arrangements, we plot the radial distribution function in Fig. 4E. The radial distribution function $g(R)$ measures the probability of finding a cell at distance R from a given reference cell. It is determined measuring the distance between all cell pairs and binning them into a histogram. The histogram ordinate is divided by R and normalized such that far away cells have $g(R) = 1$. Hence a

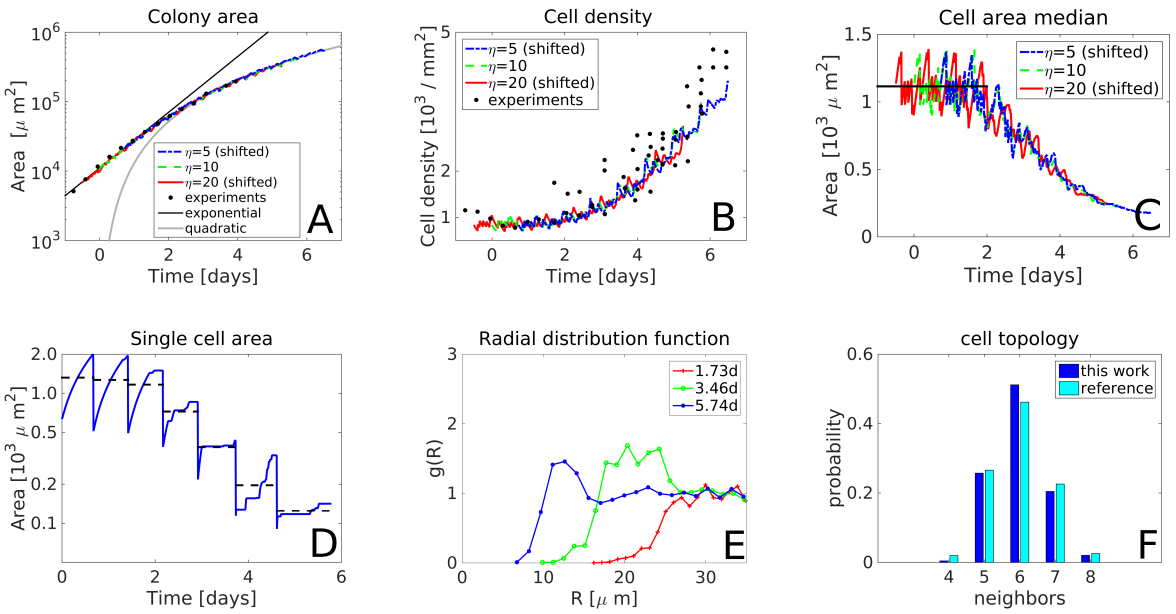

Figure 4: Analysis of cell areas and arrangements. **(A)** Total area of the spreading colony (blue). The black line corresponds to exponential growth with the average epithelial cell cycle time $0.75d$. The grey line corresponds to quadratic growth, and the symbols correspond to scaled results from the experiments in (2) (see text for additional description). The blue dot-dashed, green-dashed and the red line correspond to scaled simulation results with different mobilities η as labeled. **(B)** The corresponding average cell densities remain almost constant until $\bar{t} \approx 2d$ and grows rapidly thereafter. The plot is superimposed on the results from (2) Fig. 1 (C) with shifted time (see text). **(C)** The median of the area distribution of epithelial cells is nearly constant (indicated by solid black line) during exponential growth and shows a rapid decrease when contact inhibition sets in at $\bar{t} \approx 2d$. **(D)** Area of a single epithelial cell as a function of time remains constant before $\bar{t} \approx 2d$ and subsequently decreases afterwards. The dashed black lines are average epithelial cell areas between mitosis events. Results correspond to $\eta = 10$. **(E)** Radial distribution function of simulated cell distributions with $\eta = 10$ at different times as labelled. The appearance of a peak and trough in the quadratic growth regime indicates short-range ordering of cells. **(F)** Histogram of the distribution of the cellular coordination number (number of direct cell neighbors), with $\eta = 10$. The reference is taken from (2).

value of one indicates no correlation between the cell distances (gas-like behavior). This behavior is found in the exponential growth regime. The emergence of a peak (and a trough behind) in the quadratic growth regime indicates the development of short-range ordering of cells. This indicates the emergence of amorphous solid behavior, which is in agreement of previously found glass-like properties of growing cell clusters (3). A similar transition is observed in the experiments in (2) (see Fig. 3D).

The number of cell neighbors also referred to as 'polygon class' or 'cellular coordination number' gives another measure for the homogeneity of epithelia packings, and has been investigated in various theoretical and experimental studies, see e.g. (6, 25, 28–31) for different biological systems. In general it is found that many tissues organize such that 45% of cells have 6 neighbors, while 25% and 20% have 5 and 7 neighbors, respectively (32). Similar results are obtained in our simulations, see Fig. 4F, with 51%, 26% and 20% of 6-sided, 5-sided and 7-sided cells, respectively, again in good agreement with (2). The coordination number is measured at the final time, omitting the cells at the boundary of the colony. The standard PFC model tends to organize cells homogeneously in a hexagonal packing. This can be altered by constraints, e.g. due to an underlying curvature (33–35) or as in the present case an inhomogeneous distribution of cell sizes and the presence of mitosis. The good agreement between the simulations and experiments in (2) was achieved without any parameter adjustments.

Next, we investigate the influence of the cleavage plane, e.g., the perpendicular bisector between the two progeny at mitosis. The cleavage plane is known to have a significant influence on the arrangement of epithelial cells in models, e.g. (25), and in experiments, e.g. (32). Empirical investigations show that many monolayer cell sheets across the plant and animal kingdoms converge on a default equilibrium distribution of cellular shapes, with approximately 45% hexagons, 25% pentagons, and 20% heptagons (32). Using numerical simulations (25) found that the cell topology is

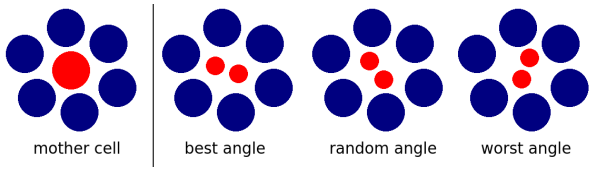

Figure 5: Schematic of different cleavage plane mechanisms. A dividing mother cell (large red circle) may align the daughters (small red circles) such that they have the most space (*best angle*), the least space (*worst angle*) or randomly (*random angle*). The blue circles denote previously existing cells.

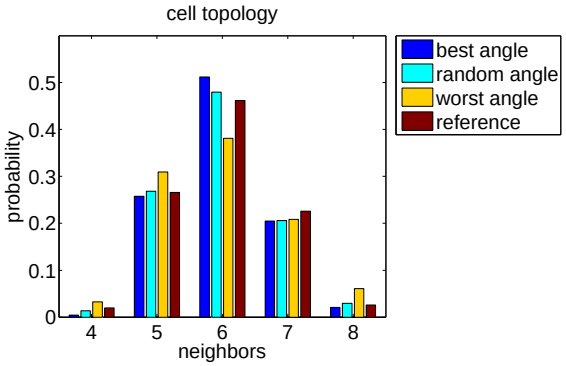

Figure 6: Histogram of the distribution of the cellular coordination number (number of direct cell neighbors) for different cleavage plane mechanisms using the mobility $\eta = 10$. The random cleavage plane produces results closest to the reference (2).

highly sensitive on the cleavage plane. In particular the number of 6-sided cells decreases for cleavage plane mechanisms from cutting the longest edge (corr. best angle) to cutting the shortest edge (corr. worst angle). We confirm this observation here using three different cleavage planes depicted in Fig. 5: The two daughter cells may be put in a position such that they have the most space (*best angle*), the least space (*worst angle*) or could be randomly aligned (*random angle*). The resulting cell coordination numbers are plotted in Fig. 6 for the various cleavage plane mechanisms. Here, we used $\eta = 10$ since our simulations revealed that the mobility η has no noticeable influence on the coordination number (results not shown).

As pointed out above the *best angle* mechanism produces a cell arrangement that is too regular (e.g., too many cells with 6 neighbors). Making the cleavage plane random leads to a more heterogeneous cell arrangement and produces cell neighbors very close to the general reference values from (2). Heterogeneity is further increased by using the *worst angle* mechanism. However, the resulting number of 6-fold cells is much lower than reported in experiments. Our results are also in qualitative agreement with the simulation results of (25). However, since their simulation does not take into account cell rearrangements they overestimate the effect of cleavage plane, which is confirmed if we compare their absolute numbers with ours. These results suggest that biological cells may indeed choose the cleavage plane in a random manner (determined by intracellular processes) since under these conditions our simulations demonstrate the closest agreement with experiments. We note that the cleavage plane has only a small influence on the total number of cells and no noticeable influence on colony area, epithelial cell density or epithelial cell areas (results not shown).

3.5 Cell motility and elastic properties

To obtain a more complete picture of the cell movements, we plot the cell velocity averaged over the last five hours of the simulation. Fig. 7 shows that cells in general move the fastest along the colony periphery while the interior cells move slowly. These outer cells migrate mostly away from the center, as expected. The inner cells move much more slowly and their movement is less oriented and more chaotic, indicating that interior motion is due primarily to cell rearrangements in the colony interior. Thus, interior cells may move past each other slowly to rearrange, a feature that is problematic to resolve with standard vertex models. The results are in general agreement with the experiments in (2), although the cell velocities found in the simulation are about 10 times smaller than those found in the experiments. This is consistent with the difference in the simulated and experimental cluster sizes and indicates that the mobility used in the simulations ($\eta = 10$) over-predicts the effects of cell-substrate adhesion (and drag).

The mechanical stress acting on the cells as has been proposed by (2) as an important step towards understanding the contact inhibition phenomenon. Here, we investigate the cell bulk stress, e.g., the compression of each cell. From the desired cell size q_i and the actual cell size $\int \chi_i dx$ we calculate the relative compression as $1 - \int \chi_i dx / q_i$. The results are shown averaged over time, according to number of neighbors and distance to the center in Fig. 8 as well as in Fig. 9 for individual cells. We find that the compression is positive for all cells and increases over time ((Fig. 8 left). Cells never occupy more space than they desire, which means they are not significantly pulled by adhesion with neighboring cells during the simulation. In the inner region the average compression is about 12.5% (Fig. 8 right) while it decays across the colony periphery to zero. The maximum compression we find is around 25%, even though cells stop growing in the simulation once they are compressed more than 10%. Hence,

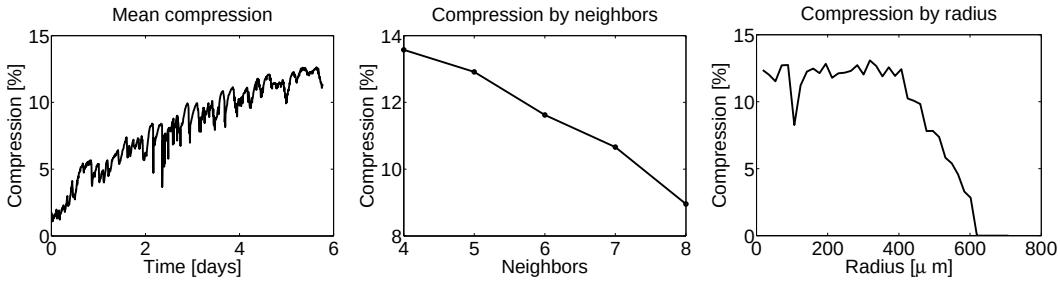

Figure 8: Cell compression as a function of time (left), number of cell neighbors (middle) and distance to the colony center (right). Results indicate that the average cell compression increases with time, cells with fewer neighbors are more compressed than cells with larger numbers of neighbors, and that cell compression is relatively constant in the inner part of the colony and decays rapidly across the outer part of the colony.

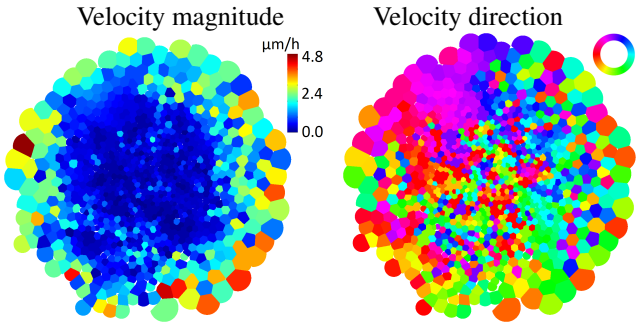

Figure 7: Cell velocity averaged over the last five hours of the simulation. **Left:** The velocity magnitude shows that cells in general move the fastest along the colony periphery while cells in the inner region move significantly more slowly. **Right:** The velocity direction is color-coded by a circular colorbar and indicates that cells in the periphery move away from the center, while inner cells have no preferred direction of movement.

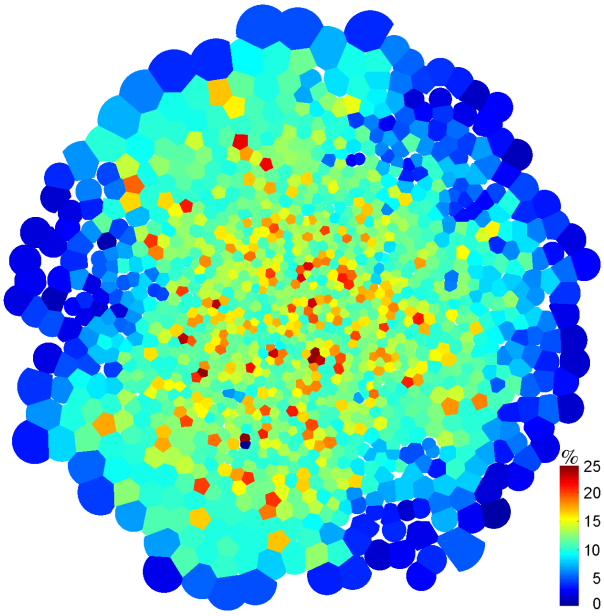

Figure 9: Compression of individual cells at the final time.

cells that are compressed more than 10% must have undergone a decrease in their area due to pressure from neighboring cells, rather than being compressed as consequence of their own growth.

Another interesting observation is the fact that cells with fewer neighbors are more compressed (Fig. 8 middle). This is consistent with reports for particle arrangements on curved surfaces, e.g. the morphology of viral capsids where the higher stress in 5-sided subunits leads to buckling, see (36) for a detailed analysis. This result is also in agreement with Lewis' law (37) which claims that cell areas are proportional to $(n-2)$ where n is the number of neighbors. Hence, if cell rearrangement decreases the number of neighbors of a certain cell, also the area of this cell is decreased leading to more compression.

4 DISCUSSION

We have presented a mechanistic model to simulate the dynamics of epithelial cell colonies. The model, which contains both continuum and discrete features, can be derived from stochastic particle models following the framework of dynamic density functional theory appropriately modified to account for cell size and shape variability and localizing approximations. Cell-cell interactions are modeled using continuum partial differential equations and cell growth and mitosis are incorporated on a discrete level. We used this model to simulate the dynamics of clusters of epithelial cells to quantify contact inhibition dynamics at the tissue and single cell levels.

To validate the appropriateness of the model, we compared the simulated results with the detailed in vitro studies

of epithelial tissue dynamics of Madin-Darby canine kidney (MDCK) cells in (2). We found that the model correctly predicts a transition in the growth of the colony sizes from exponential at early times to quadratic at later times. The transition occurs because of reduced cell movement and the lack of space that prevents cells in the cluster interior from growing in size (although they may still undergo reductive cell division) while cells in the cluster exterior move and grow more freely, which provide the source of cluster size increases at later times. The transition is also associated with the emergence of short-range ordering and solid-like behavior of the cluster, which was quantified using the radial distribution function, and a constant-thickness growing (and dividing) rim of cells at the cluster edge. In the simulations, the mobility, which reflects the combined effects of cell-substrate adhesion and drag, and the Young's modulus are the primary influences on the transition from exponential to quadratic growth with an increased mobility (or Young's modulus) being associated with a delayed onset of the transition because the cells are more mobile (or stiff) resulting in an extension of the free-growth regime. For the range of mobilities used, the model under-predicts the cluster sizes where the transition occurs. Computational costs prevented us from using significantly larger values of these parameters. However, an analysis of the results reveals a scale-invariance such that the appropriately scaled simulation and experimental results are in excellent agreement. Excellent agreement is also obtained for the evolution of cell densities and cell sizes. We further investigated the distributions of the cellular coordination numbers (number of cell neighbors), the average cell velocity and the mechanical stress. We found that the cleavage plane is the dominant mechanism to control cell topology but has little effect on the colony morphologies or growth. The experiments are most consistent with randomly chosen cleavage planes. The local stress is found to depend on the cell coordination numbers with fewer neighbors resulting in larger stresses, consistent with Lewis' law (37) . In addition, cells in the cluster interior are found to be much more compressed and to move much more slowly and in more random directions than their exterior counterparts. Taken all together, our results confirm the findings of (2) identifying contact inhibition as a consequence of mechanical constraints that cause successive cell divisions to reduce the cell area and is not just a result of cell contact.

Compared to previous models, our approach has several advantages: (i) because of the continuum formulation, cell-cell interactions can be simulated efficiently using sophisticated partial differential equation solvers, (ii) the model can capture elastic, viscoelastic and plastic deformations within this continuum framework; (iii) the model is dimension independent, (iv) the model can easily be extended to incorporate multiple cell types, general substrate geometries and the dependence of cell behavior on oxygen, nutrients and growth factors, and (v) the model can be parametrized using classical elastic properties (e.g., Poisson's ratio and Young's modulus).

Although the elastic properties of cell colonies are in principle measurable, these elastic parameters are not well-known. In contrast, the mechanical properties of individual cells, which can be measured by Atomic Force Microscopy (AFM) probe indentation, e.g., see (38), are much better known. To derive the Young's modulus of an individual cell from such indentation experiments, simple mechanical models are typically used (39). Values for human cervical epithelial cells range from $1 - 20kPa$, depending on the indentation experiment and the mechanical model considered. How these properties for single cells can be related to the mechanical properties of cell colonies remains open. However, another advantage of our approach is that our model can also be parametrized using an experimentally-derived direct two-point correlation function to start with (recall the model derivation in Sec. 2). For example, experimental measurements can provide an approximation of the dynamic structure factor (e.g., (3)). By solving the Ornstein-Zernike integral equation (e.g., (40)), we can approximate the direct two-point correlation function from the structure factor. We plan to consider this in future work.

Author contributions A.V. and J.L. originated the overall design of the research. S.A. conducted the mathematical modeling and numerical study. S.A., A.V. and J.L. analysed the results and wrote the paper. H.H. contributed in the critical discussions of the model's biological applications and the corresponding parametrisation.

Acknowledgements S.A., H.H. and A.V. acknowledge support from the German Science Foundation within SPP 1506 Al1705/1, SPP 1296 Vo899/7 and EXC CfAED as well as the European Commission within FP7-PEOPLE-2009-IRSES PHASEFIELD, which J.L. also acknowledges. J.L. is grateful for support from the National Science Foundation Division of Mathematical Sciences and from the National Institutes of Health through grant P50GM76516 for a Center of Excellence in Systems Biology at the University of California, Irvine and grant P30CA062203 for the Chao Family Comprehensive Cancer Center at UC Irvine. Simulations were carried out at ZIH at TU Dresden, JSC at FZ Julich and at UC Irvine. S.A. also thanks the hospitality of the Department of Mathematics at the University of California, Irvine where some of this research was conducted. The authors also thank Zhen Guan for helpful discussions regarding the numerical methods.

SUPPLEMENTARY MATERIAL

An online supplement to this article can be found by visiting BJ Online at http://www.biophysj.org., which includes analysis of a one-mode approximation to determine the chosen parameters and a movie of the growth process.

References

1. Vincent, J.-P., A. G. Fletcher, and L. A. Baena-Lopez, 2013. Mechanisms and mechanics of cell competition in epithelia. Nature Reviews Molecular Cell Biology 14:581–591.
2. Puliafito, A., L. Hufnagel, P. Neveu, S. Streichan, A. Sigal, D. K. Fygenson, and B. I. Shraiman, 2012. Collective and single cell behavior in epithelial contact inhibition. Proceedings of the National Academy of Sciences 109:739–744.
3. Angelini, T., E. Hannezo, X. Trepat, M. Marquez, J. Fredberg, and D. Weitz, 2011. Glass-like dynamics of collective cell migration. Proc. Nat. Acad. USA 108:4714–4719.
4. Shraiman, B. I., 2005. Mechanical feedback as a possible regulator of tissue growth. Proceedings of the National Academy of Sciences 102:3318–3323.
5. Scianna, M., and L. Preziosi, 2012. Multiscale developments of the Cellular Potts model. Math. Model. Nat. Phenom. 7:78–104.
6. Farhadifar, R., J.-C. Röper, B. Aigouy, S. Eaton, and F. Jülicher, 2007. The influence of cell mechanics, cell-cell interactions, and proliferation on epithelial packing. Current Biology 17:2095–2104.
7. Li, J., and J. Lowengrub, 2014. The effects of cell compressibility, motility and contact inhibition on the growth of tumor cell clusters using the Cellular Potts model. J. Theor. Biol. 343:79–91.
8. Landsberg, K. P., R. Farhadifar, J. Ranft, D. Umetsu, T. J. Widmann, T. Bittig, A. Said, F. Jülicher, and C. Dahmann, 2009. Increased cell bond tension governs cell sorting at the Drosophila anteroposterior compartment boundary. Current Biology 19:1950–1955.
9. Wartlick, O., P. Mumcu, A. Kicheva, T. Bittig, C. Seum, F. Jülicher, and M. Gonzalez-Gaitan, 2011. Dynamics of Dpp signaling and proliferation control. Science 331:1154–1159.
10. Vogel, V., and M. Sheetz, 2006. Local force and geometry sensing regulate cell functions. Nature Reviews Molecular Cell Biology 7:265–275.
11. Rauzi, M., P.-F. Lenne, and T. Lecuit, 2010. Planar polarized actomyosin contractile flows control epithelial junction remodelling. Nature 468:1110–1114.
12. Hannezo, E., J. Prost, and J.-F. Joanny, 2014. Theory of epithelial sheet morphology in three dimensions. Proceedings of the National Academy of Sciences 111:27–32.
13. Sepulveda, N., L. Petitjean, O. Cochet, E. Grasland-Mongrain, P. Silberzan, and V. Hakim, 2013. Collective cell motion in an epithelial sheet can be quantitatively described by a stochastic interacting particle model. PLoS Computational Biology 9:e1002944.
14. Macklin, P., M. Edgerton, A. Thompson, and V. Cristini, 2012. Patient-calibrated agent-based modeling of ductal carcinoma in situ (DCIS): From microscopic measurements to macroscopic predictions of clinical progression. J. Theor. Biol. 301:122–140.
15. Poujade, M., E. Grasland-Mongrain, A. Hertzog, J. Jouanneau, P. Chavrier, B. Ladoux, A. Buguin, and P. Silberzan, 2007. Collective migration of an epithelial monolayer in response to a model wound. Proceedings of the National Academy of Sciences 104:15988–15993.
16. Petitjean, L., M. Reffay, E. Grasland-Mongrain, M. Poujade, B. Ladoux, A. Buguin, and P. Silberzan, 2010. Velocity fields in a collectively migrating epithelium. Biophysical Journal 98:1790–1800.
17. Chauviere, A., H. Hatzikirou, I. G. Kevrekidis, J. S. Lowengrub, and V. Cristini, 2012. Dynamic density functional theory of solid tumor growth: Preliminary models. AIP Advances 2:011210.
18. Marconi, U. M. B., and P. Tarazona, 1999. Dynamical density functional theory of liquids. Journal of Chemical Physics 110:8032–8044.
19. Archer, A. J., and R. Evans, 2004. Dynamical density functional theory and its application to spinodal decomposition. Journal of Chemical Physics 121:4246–4254.
20. Elder, K., N. Provatas, J. Berry, P. Stefanovic, and M. Grant, 2007. Phase-field crystal modeling and classical density functional theory of freezing. Physical Review B 75:064107.
21. van Teeffelen, S., R. Backofen, A. Voigt, and H. Löwen, 2009. Derivation of the phase-field-crystal model for colloidal solidification. Physical Review E 79:051404.
22. Elder, K., M. Katakowski, M. Haataja, and M. Grant, 2002. Modeling elasticity in crystal growth. Physical Review Letters 88:245701.
23. Chan, P. Y., N. Goldenfeld, and J. Dantzig, 2009. Molecular dynamics on diffusive time scales from the phase-field-crystal equation. Physical Review E 79:035701.
24. Praetorius, S., and A. Voigt, 2011. A phase field crystal approach for particles in a flowing solvent. Macromolecular Theory and Simulations 20:541–547.
25. Patel, A. B., W. T. Gibson, M. C. Gibson, and R. Nagpal, 2009. Modeling and inferring cleavage patterns in proliferating epithelia. PLoS Computational Biology 5:e1000412.
26. Wise, S., C. Wang, and J. S. Lowengrub, 2009. An energy-stable and convergent finite-difference scheme for the phase field crystal equation. SIAM Journal on Numerical Analysis 47:2269–2288.
27. Hu, Z., S. Wise, C. Wang, and J. S. Lowengrub, 2009. Stable and efficient finite-difference nonlinear-multigrid schemes for the phase field crystal equation. Journal of Computational Physics 228:5323–5339.
28. Aegerter-Wilmsen, T., A. C. Smith, A. J. Christen, C. M. Aegerter, E. Hafen, and K. Basler, 2010. Exploring the effects of mechanical feedback on epithelial topology. Development 137:499–506.
29. Staple, D., R. Farhadifar, J.-C. Röper, B. Aigouy, S. Eaton, and F. Jülicher, 2010. Mechanics and remodelling of cell packings in epithelia. The European Physical Journal E 33:117–127.
30. Axelrod, J. D., 2006. Cell shape in proliferating epithelia: a multifaceted problem. Cell 126:643–645.
31. Nagpal, R., A. Patel, and M. C. Gibson, 2008. Epithelial topology. BioEssays 30:260–266.
32. Gibson, W. T., J. H. Veldhuis, B. Rubinstein, H. N. Cartwright, N. Perrimon, G. W. Brodland, R. Nagpal, and M. C. Gibson,

2011. Control of the mitotic cleavage plane by local epithelial topology. Cell 144:427–438.
33. Backofen, R., T. Witkowski, and A. Voigt, 2010. Particles on curved surfaces - a dynamic approach by a phase field crystal model. Physical Review E 81:025701.
34. Backofen, R., M. Gräf, D. Potts, S. Praetorius, A. Voigt, and T. Witkowski, 2011. A continuous approach to discrete ordering on S^2. Multiscale Modeling and Simulation 9:314–334.
35. Schmid, V., and A. Voigt, 2014. Crystalline order and topological charges on capillary bridges. Soft Matter 10:4694–4699.
36. Aland, S., A. Rätz, M. Röger, and A. Voigt, 2012. Buckling instability of viral capsids - a continuum approach. SIAM MMS 10:82–110.
37. Lewis, F., 1928. The correlation between cell division and the shapes and sizes of prismatic cells in the epidermis of cucumis. Anat. Rec. 38:3412–376.
38. Sokolov, I., M. Dokukin, and N. Guz, 2013. Method for quantitative measurements of the elastic modulus of biological cells in AFM indentation experiments. Methods 60:202–213.
39. Guz, N., M. Dokukin, V. Kalaparthi, and I. Sokolov, 2014. If Cell Mechanics Can Be Described by Elastic Modulus: Study of Different Models and Probes Used in Indentation Experiments. Biophysical Journal 107:564.
40. Caccamo, C., 1996. Integral equation theory description of phase equilibria in classical fluids. Phys. Rep. 274:1–105.
41. Elder, K., and M. Grant, 2004. Modeling elastic and plastic deformations in nonequilibrium processing using phase field crystals. Phys. Rev. E 70:051605.
42. Mertz, A., S. Banerjee, Y. Che, G. German, Y. Xu, C. Hyland, M. Marchetti, V. Horsley, and E. Dufresne, 2012. Scaling of Traction Forces with the Size of Cohesive Cell Colonies. Phys. Rev. Lett. 108:198101.
43. Mumford, D., and J. Shah, 1989. Optimal approximations by piecewise smooth functions and associated variational problems. Communications on Pure and Applied Mathematics 42:577–685.
44. Berkels, B., A. Rätz, M. Rumpf, and A. Voigt, 2008. Extracting grain boundaries and macroscopic deformations from images on atomic scale. Journal of Scientific Computing 35:1–23.
45. Backofen, R., and A. Voigt, 2014. A phase field crystal study of heterogeneous nucleation - Application of the string method. European Physical Journal - Special Topics 223:497–509.

SUPPLEMENTARY MATERIAL

One-mode approximation

A detailed analysis of the standard PFC model in Eq. (2) was performed in (41) for the case of $q = 1$. For $q = const$ the analysis follows along the same lines. We can represent the periodic solution by a one-mode approximation with the lowest-order harmonic expansion

$$\rho = A(\cos(2\pi x/a)\cos(2\pi y/\sqrt{3}a) - \cos(2\pi y/\sqrt{3}a)/2) + \rho_0$$

where ρ_0 is the average epithelial cell density, A measures the amplitude of the epithelial cell density field and a is the distance between the cells. Recall that the density ρ actually represents the deviation from a reference value $\bar{\rho}$ (see Sec. 2). Using this expression in the PFC energy in Eq. (1) and minimizing with respect to A and a leads to

$$A = \frac{4}{5}\left(\rho_0 - \frac{1}{3}\sqrt{-15r - 36\rho_0^2}\right), \quad a = \frac{4\pi}{\sqrt{3}}\sqrt{q}.$$

Hence the distance between cells scales with the square root of q, whereas the amplitude of the epithelial cell density field is not affected by q. The maxima of the above one-mode approximation are easily calculated as $\rho_{\text{peak}} = \rho_0 - 1.5A$. We will use this value as ρ_{max}.

We can obtain the elastic properties of the hexagonal phase from the one-mode approximation by considering the energy cost of a deformation of the equilibrium state following (41). The resulting elastic constants are $C_{11}/3 = C_{12} = C_{44} = 3A^2/16$, independent of q. From these coefficients, we obtain the Poisson ratio $\nu = 1/3$ and the Young's modulus $E = A^2/2$. These calculations are only valid within the one-mode approximation, assuming a perfectly hexagonal packing of the epithelial cells. As shown in (41) these approximations are in good agreement with the elastic properties obtained from the full PFC model, at least if r is small. In the simulations presented in this paper, we are within this regime, but far away from an equilibrium hexagonal state, which should be kept in mind by parametrizing the model according to experimental measurements of E.

Mechanical properties of epithelial cell colonies have previously been considered in (42) within a one-dimensional approach by using a homogeneous and isotropic material, parametrized by ν and E. However, in (42) the cells are coupled to a substrate and therefore the results can not be compared with our simulations in the current setting. The fixed Poisson ratio is within the range $0.3-0.5$ of typical soft materials (39). Using $r = -0.9$ and $\rho_0 = -0.54$ we obtain $E = 0.4$. Below, we demonstrate the effects of changing the Young's modulus E (see Fig. SI.3).

Phase diagram

By comparing the free energies (for constant q) of a hexagonal cell ordering in equilibrium and a constant density, a

h

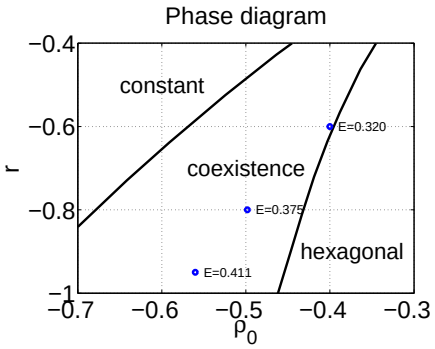

Figure SI.1: The phase diagram for the phase field crystal model. The region labelled "coexistence" marks the ranges of the parameters r and ρ_0 where regions with hexagonal cell ordering in equilibrium can coexist with regions with constant density (e.g., no cells). Note that ρ_0 actually represents the deviation from a reference value $\bar{\rho}$ (recall Sec. 2). The blue circles indicate the three distinct parameter combinations together with the corresponding Young's moduli.

phase diagram can be constructed. The phase diagram is shown in Fig. SI.1) in terms of the parameters ρ_0 and r. There are three phases: (i) constant density phases where there are no cells; (ii) coexistence phases where regions of hexagonally-arranged cells can coexist in equilibrium with regions where there are no cells; and (iii) hexagonal phases where there are only hexagonally-arranged cells in equilibrium. Results are independent of q.

Parameter variation

We next demonstrate how the results of our simulations depend on the model parameters, including the mobility, the choice of cleavage plane, and the Young's modulus.

Effect of mobility and cleavage plane. Fig. SI.2 shows the epithelial cell colony at final time $t = 5.77d$ for various parameter combinations. The cleavage plane seems to have little impact on the colony morphologies (top) or the total number of cells (Fig. SI.2A). The only noticeable influence is on the colony boundary, which seems more rough for the worst angle of the cleavage plane (recall Fig. 5). The colony boundary is extracted from the epithelial cell density field ρ, or the discrete representation χ_i, using a segmentation algorithm based on a Mumford-Shah energy (43) with the initial noisy representation of the colony defined by $1 - \chi_0$. This approach was shown to be robust for crystalline materials in (44, 45) and works well also in the present situation.

The most striking observation from Fig. SI.2 is that the cell colony grows larger with increasing mobility since a larger mobility makes it easier for the cells to move. Fig. SI.2B shows that increasing the mobility delays the transition from exponential to quadratic growth making the transition occur at larger cell populations. Accordingly, the the epithelial cell density (Fig. SI.2C) and the median of the epithelial cell area (Fig. SI.2D) remain constant for a longer time. Hence larger mobilities lead to a longer free-growth regime. A larger mobility makes it easier for the bulk epithelial cells to push outer cells aside to gain enough space to grow. Thus, bulk epithelial cells are less compressed and contact inhibition sets in later than for lower mobilities. The longer lasting exponential growth is not only reflected by the total colony area but also by the increased total number of epithelial cells for larger η (Fig. SI.2A). As shown in Fig. 4 in the main text, the results collapse onto a single curve when plotted against a shifted time $\bar{t}$ and the colony size is rescaled. Accordingly, $t_{shift} = 16$h, -24h and $A_{ref} = 0.41, 3.79$ for $\eta = 5, 20$, respectively.

Effect of elastic parameters To demonstrate the influence of E on our results we also consider $r = -0.6, -0.8, -0.95$ and keep $\rho_{\text{peak}} = 0.8$ fixed, which results in a change of ρ_0 depending on ρ_{peak} as indicated above. The resulting Young's moduli are $E = 0.320, 0.375, 0.411$, respectively. The three distinct parameter sets are marked in the phase diagram in Fig. SI.3. All parameter sets are within the coexistence regime of the hexagonal phase and a constant phase.

Simulation results in Fig. SI.1 shows that increasing E delays the transition from exponential to quadratic growth by increasing the ability of cells to push each other. This extends the free-growth regime in a manner analogous to that observed when the mobility is increased. As shown in Figs. SI.1B and D, the results still collapse onto a single curve when plotted against a shifted time $\bar{t}$ and with rescaled colony size. Accordingly, $t_{shift} = 0.6$d, 0.2d and $A_{ref} = 0.45, 0.77$ for $E = 0.32, 0.375$, respectively.

Movie

We provide a movie showing the evolution of the colony in the reference configuration ($\eta = 10$, best angle). Time is scaled with a factor of 21.8h/s.

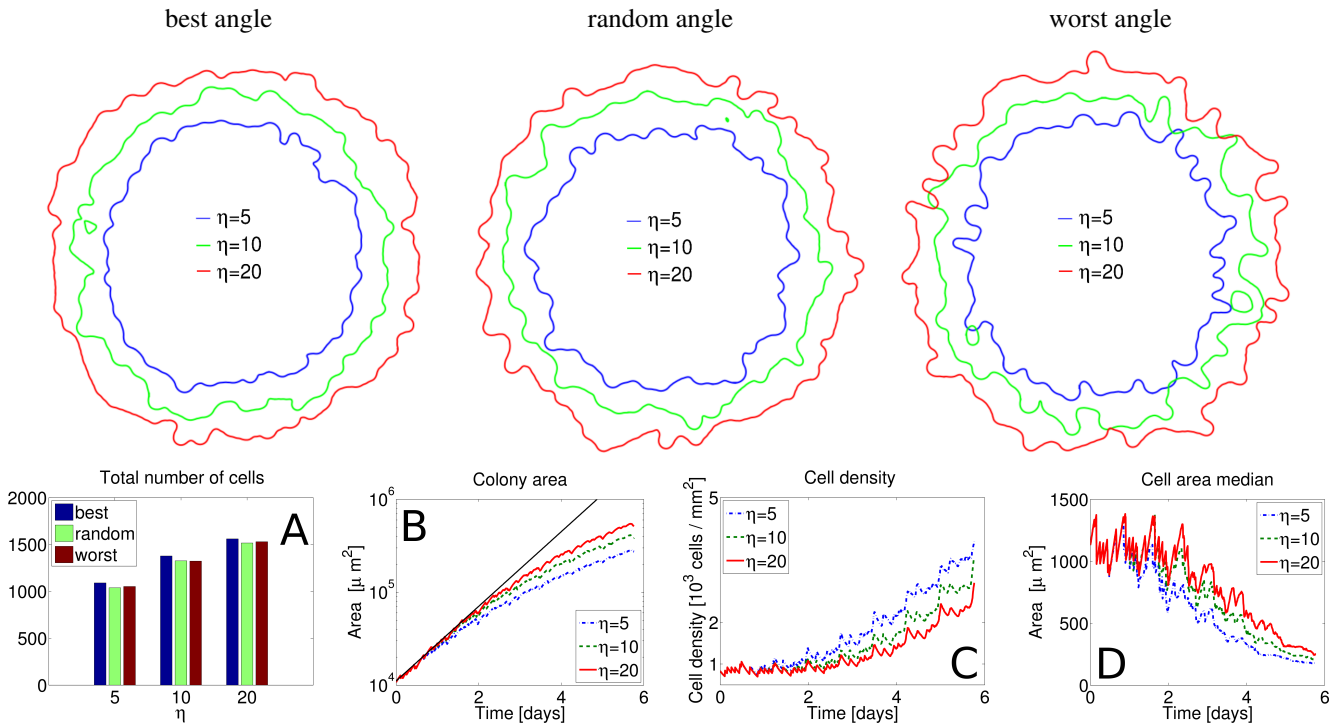

Figure SI.2: (Top row:) Epithelial cell colony morphologies at final time $t = 5.77d$ for different cleavage planes (*best,random* and *worst angle* (from left to right) and mobilities ($\eta = 5, 10, 20$ plotted together, (**A**) The total number of cells at final time for different cleavage planes and mobilities. (**B**) Total area of the spreading colony. The solid black line corresponds exponential growth with average cell cycle time $0.75d$, (**C**) Average cell density for different mobilities, (**D**) Median of cell area distribution. Since the cleavage plane was found to have little influence, results in (**B**), (**C**) and (**D**) are shown for the *best angle* mechanism only.

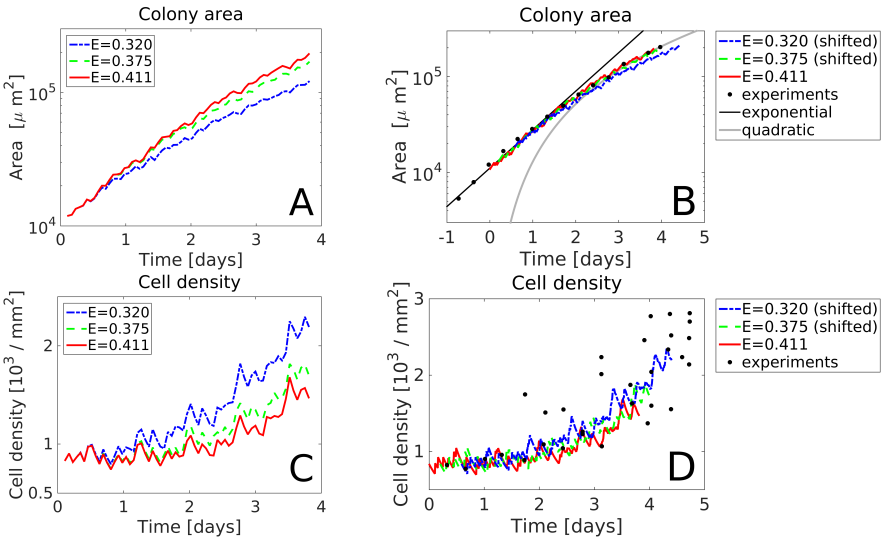

Figure SI.3: Colony area (**A**) and cell density (**C**) for different values of the Young's modulus of the epithelial cell cluster. Results collapse on one another when plotted in rescaled variables (see text) in (**C**) and (**D**) and show excellent agreement with experiments from (2) (see text).